

Structure-Informed Estimation for Pilot-Limited MIMO Channels via Tensor Decomposition

Alexandre Barbosa de Lima¹

¹Faculty of Exact Sciences and Technology, Pontifical Catholic University of São Paulo (PUC-SP), São Paulo, Brazil
Email: ablima@pucsp.br

March 3, 2026

Abstract

Accurate channel state information in wideband multiple-input multiple-output (MIMO) systems is fundamentally constrained by pilot overhead, a challenge that intensifies as antenna counts and bandwidths scale toward 6G. This paper proposes a structure-informed hybrid estimator that formulates pilot-limited MIMO channel estimation as low-rank tensor completion from sparse pilot observations—a severely underdetermined inverse problem that prior tensor approaches avoid by assuming fully observed received signal tensors. Canonical polyadic (CP) and Tucker decompositions are comparatively analyzed: CP excels for specular channels whose rank-one multipath structure matches the CP parameterization exactly, while Tucker provides greater numerical stability at extreme pilot scarcity where CP exhibits heavy-tail divergence. A lightweight 3D U-Net learns residual components beyond the dominant low-rank structure, compensating for diffuse scattering and hardware non-idealities that algebraic priors alone cannot capture. On synthetic specular channels, Tucker completion achieves 10.88 dB NMSE improvement over least squares and 7.83 dB over orthogonal matching pursuit at $\rho = 10\%$ pilot density; CP outperforms Tucker by 13.11 dB at SNR = 20 dB under the specular multipath model. On DeepMIMO ray-tracing channels, the hybrid estimator surpasses CP by 2.26 dB and Tucker by 4.80 dB at $\rho = 8\%$, while remaining stable at $\rho = 2\%$ where CP diverges; algebraic structure consistently outperforms unconstrained deep learning across the full pilot-density range, with a margin growing from 1.53 dB at $\rho = 2\%$ to 5.67 dB at $\rho = 20\%$. Empirical recovery threshold analysis confirms that sample complexity scales with intrinsic channel dimensionality—governed by the number of dominant propagation paths—rather than with the ambient tensor size.

Keywords: MIMO channel estimation, tensor decomposition, structure-informed learning, low-rank recovery, pilot overhead reduction.

1 Introduction

Wideband multiple-input multiple-output (MIMO) systems with large antenna arrays are fundamental enablers of high-capacity wireless links in 5G and beyond networks. Point-to-point MIMO configurations are particularly relevant for wireless backhaul, fixed wireless access, vehicle-to-infrastructure communications, and satellite feeder links [1, 2]. However, the spectral efficiency gains from spatial multiplexing critically depend on accurate channel state information (CSI), whose acquisition becomes progressively challenging as antenna counts, bandwidth, and mobility increase [3].

Recent advances in radio-frequency (RF) integration have fundamentally altered the architectural landscape of large-array systems. Fully digital transceivers—once considered impractical at millimeter-wave frequencies—are now recognized as scalable and energy-efficient, with commercial deployments already underway at sub-6 GHz and expected at millimeter-wave (mmWave) frequencies [4]. This architectural shift is further motivated by emerging 6G use cases such as Integrated Sensing and Communications (ISAC), where fine-grained, per-antenna access to received signals is essential for joint optimization across communication and sensing tasks [5]. The present article focuses on fully digital MIMO orthogonal frequency-division multiplexing (MIMO-OFDM) architectures with direct baseband access to individual antenna-domain channel coefficients.

Conventional estimation techniques such as least squares (LS) and linear minimum mean-square error (LMMSE) require pilot resources scaling with channel dimensionality. In wideband MIMO-OFDM systems, the channel comprises $N_r N_t N_f$ complex coefficients, where N_r , N_t , and N_f denote the number of receive antennas, transmit antennas, and subcarriers, respectively, translating to tens of thousands of unknowns for systems with tens of antennas and hundreds of subcarriers [6, 7]. Deep learning addresses pilot scarcity by learning nonlinear mappings from sparse observations to full reconstructions [8–12], achieving strong performance when training and deployment conditions match. However, these methods typically require large labeled datasets, offer limited interpretability, and generalize poorly under distribution shifts—limitations particularly pronounced in pilot-limited regimes. A fundamental challenge lies in the limited availability of representative training data: unlike computer vision or natural language processing (NLP), acquiring labeled physical-layer data from operational networks is costly and often impractical [4].

Physics-informed learning mitigates generalization issues by embedding prior knowledge through constraints or regularization [13], often via ray tracing or site-specific geometric models [14, 15]. Although effective in controlled settings, these approaches depend on detailed environmental information and scale poorly across heterogeneous deployments. This paper adopts a complementary perspective: exploiting algebraic structure as a universal physical prior. Rather than encoding propagation physics through explicit geometry, algebraic constraints enforce low rank, separability, and multilinear structure arising from fundamental scattering mechanisms—properties that emerge universally from sparse multipath propagation and array geometry, making them portable across deployment scenarios [1, 2, 7]. In wideband systems, these properties combine into hierarchical spatial–frequency correlations naturally captured by tensor decompositions [16–18].

A comparison between tensor completion and compressed sensing (CS) highlights key structural differences. CS-based approaches assume sparsity in a predefined angular–delay dictionary and recover coefficients from linear measurements, but are susceptible to basis mismatch in off-grid scenarios. Tensor completion instead exploits low-dimensional multilinear structure—such as canonical polyadic (CP) or Tucker rank—directly in the native antenna–frequency domain without explicit dictionary construction. These perspectives are complementary: sparsity captures parametric specular structure, while multilinear low-rank models capture broader correlations and offer robustness under richer scattering conditions.

Prior tensor-based channel estimation has demonstrated substantial gains. Zhou et al. [17] formulated mmWave estimation as CP decomposition of a fully observed received signal tensor after RF combining—an overdetermined problem targeting hybrid architectures. Tensor methods have also found application in MIMO relay systems via nested Tucker decompositions [19] and in time-varying channels under high mobility [20]. However, these formulations assume fully observed tensors and do not address pilot-limited completion.

This paper addresses a complementary scenario: pilot-limited estimation in fully digital systems where only a sparse subset of channel tensor entries is observed. This severely underdetermined inverse problem requires regularization through low-rank tensor completion—a fundamentally different mathematical setting applicable to a broader class of MIMO-OFDM systems [4].

The main contributions of this article are:

1. **Tensor completion formulation for pilot-limited MIMO:** Unlike prior methods assuming fully observed tensors [17], this work formulates the problem as tensor completion from sparse pilot samples.
2. **Hybrid tensor–neural architecture:** A two-stage estimator combining low-rank tensor completion with neural residual learning, achieving 1–5 dB NMSE reduction over pure tensor-based methods on DeepMIMO ray-tracing channels, with the hybrid estimator remaining stable under extreme pilot scarcity where CP-based methods exhibit numerical instability.
3. **Comprehensive validation:** Evaluation against LS and OMP baselines demonstrates 7–11 dB NMSE improvement at 5–10% pilot density on synthetic channels, and up to 14 dB on DeepMIMO ray-tracing channels at comparable pilot densities.

The remainder of this paper is organized as follows. Section 2 introduces the system and channel models. Section 3 presents tensor representations and algebraic priors. Section 4 describes the estimation framework. Section 5 presents simulation results. Section 6 concludes the paper.

2 System Model

This paper denotes scalars by lowercase letters (e.g., α), vectors by bold lowercase letters (e.g., \mathbf{a}), matrices by bold uppercase letters (e.g., \mathbf{A}), and tensors by calligraphic letters (e.g., \mathcal{H}). The wideband MIMO channel takes the form of a third-order tensor $\mathcal{H} \in \mathbb{C}^{N_r \times N_t \times N_f}$, where $\mathbf{w}[k]$ denotes the k -th entry of a vector \mathbf{w} . The symbol \circ denotes the outer product, \times_n the n -mode product, $\|\cdot\|_F$ the Frobenius norm, \odot the Hadamard (element-wise) product, \otimes the Kronecker product, and $(\cdot)^H$ the conjugate transpose (adjoint). All tensor dimensions and ranks follow this convention throughout the paper.

Let $\mathbf{H}[k] \in \mathbb{C}^{N_r \times N_t}$ denote the frequency-domain channel matrix at subcarrier $k \in \{1, \dots, N_f\}$. The received signal satisfies

$$\mathbf{y}[k] = \mathbf{H}[k]\mathbf{x}[k] + \mathbf{n}[k], \quad (1)$$

where $\mathbf{x}[k] \in \mathbb{C}^{N_t}$ is the transmitted signal vector and $\mathbf{n}[k] \sim \mathcal{CN}(\mathbf{0}, \sigma^2 \mathbf{I})$ denotes additive white Gaussian noise [21].

2.1 Pilot-Based Channel Estimation

During the training phase, known pilot symbols occupy a subset of resource elements (i, j, k) of the channel tensor, so observations cover only a subset of its coefficients. Stacking the frequency-domain channel matrices $\mathbf{H}[k] \in \mathbb{C}^{N_r \times N_t}$ across all N_f subcarriers yields the wideband MIMO channel as a third-order tensor

$$\mathcal{H} \in \mathbb{C}^{N_r \times N_t \times N_f}. \quad (2)$$

Pilot-based acquisition covers only the subset of tensor entries indexed by

$$\Omega \subset \{1, \dots, N_r\} \times \{1, \dots, N_t\} \times \{1, \dots, N_f\}. \quad (3)$$

The resulting observation model reads [17]

$$\mathcal{Y}_\Omega = \mathcal{P}_\Omega(\mathcal{H} + \mathcal{N}) = \mathcal{P}_\Omega(\mathcal{H}) + \mathcal{P}_\Omega(\mathcal{N}), \quad (4)$$

where $\mathcal{P}_\Omega(\cdot)$ denotes the entry-wise sampling operator in (5)

$$[\mathcal{P}_\Omega(\mathcal{H})]_{ijk} = \begin{cases} \mathcal{H}_{ijk}, & \text{if } (i, j, k) \in \Omega, \\ 0, & \text{otherwise,} \end{cases} \quad (5)$$

and \mathcal{N} is i.i.d. complex Gaussian noise. In practical pilot-aided OFDM training, the channel tensor admits no direct observation. At each pilot location $(i, j, k) \in \Omega$, a known pilot symbol provides a noisy scalar observation of the corresponding channel coefficient \mathcal{H}_{ijk} . Accordingly, $\mathcal{P}_\Omega(\mathcal{H})$ collects these observations as entry-wise samples of the channel tensor corrupted by additive noise. This abstraction reduces the estimation problem to entry-wise sampling of the channel tensor with noise, which is standard in tensor completion and isolates the impact of pilot sparsity from waveform-specific effects. This article defines SNR with respect to the average power per channel coefficient over the full tensor \mathcal{H} , independent of the pilot set Ω and pilot ratio ρ , as formalized in (16). This ensures strict SNR comparability across all pilot densities. Equivalently, $\mathcal{P}_\Omega(\mathcal{H}) = \mathcal{M} \odot \mathcal{H}$, where $\mathcal{M} \in \{0, 1\}^{N_r \times N_t \times N_f}$ is a binary mask with $[\mathcal{M}]_{ijk} = 1$ if $(i, j, k) \in \Omega$. Stacking the per-subcarrier noise vectors $\mathbf{n}[k]$ across receive antennas and frequency indices yields the noise tensor \mathcal{N} , consistently with (1). This article defines SNR with respect to the average power per channel coefficient over the full tensor \mathcal{H} , independent of the pilot set Ω and pilot ratio ρ , as formalized in (16). This ensures strict SNR comparability across all pilot densities. Equivalently, $\mathcal{P}_\Omega(\mathcal{H}) = \mathcal{M} \odot \mathcal{H}$, where $\mathcal{M} \in \{0, 1\}^{N_r \times N_t \times N_f}$ is a binary mask with $[\mathcal{M}]_{ijk} = 1$ if $(i, j, k) \in \Omega$. Stacking the per-subcarrier noise vectors $\mathbf{n}[k]$ across receive antennas and frequency indices yields the noise tensor \mathcal{N} , consistently with (1).

The tensor completion formulation treats pilot-limited observation as entry-wise sampling over an index set Ω . The experiments draw Ω from a pilot mask with either random sampling, a regular grid, or a comb pattern in frequency. Random uniform sampling serves as the default model, consistent with standard practice in tensor completion literature [26, 33]. Structured masks define deterministic index sets that satisfy the same observation model but may exhibit different empirical recovery behavior; their performance is assessed experimentally in Experiment 4.

When the pilot ratio (ρ) satisfies

$$\rho = \frac{|\Omega|}{N_r N_t N_f} \ll 1, \quad (6)$$

only a small fraction of channel tensor coefficients admits direct observation. In this pilot-limited regime, recovering the full channel tensor \mathcal{H} from partial and noisy observations \mathcal{Y}_Ω constitutes a severely ill-posed inverse problem: unknowns vastly exceed measurements, the observation operator is highly rank-deficient, and the solution is non-unique and noise-sensitive [6, 7, 22]. This fundamental limitation motivates incorporating structural priors that exploit intrinsic spatial and spectral correlations of the channel to regularize the estimation problem and enable reliable reconstruction.

2.2 Multipath Channel Model

In sparse scattering environments—such as outdoor deployments with limited reflectors or higher-frequency bands—wireless propagation is typically dominated by a small number of specular paths, leading to low-rank multipath channels [2]. Under this assumption, the frequency-domain channel at subcarrier k admits the geometric representation

$$\mathbf{H}[k] = \sum_{\ell=1}^L \alpha_\ell \mathbf{a}_r(\theta_\ell) \mathbf{a}_t^H(\phi_\ell) e^{-j2\pi k \tau_\ell}, \quad k = 1, \dots, N_f, \quad (7)$$

where L denotes the number of dominant propagation paths, $\alpha_\ell \in \mathbb{C}$ are complex path gains, $\mathbf{a}_r(\theta_\ell)$ and $\mathbf{a}_t(\phi_\ell)$ are receive and transmit array steering vectors associated with angles of arrival and departure, respectively, assuming a 2D propagation model with azimuth-only angular parameters, and $\tau_\ell \in [0, 1)$ represents the normalized propagation delay. The exponential term models frequency-dependent phase rotation induced by path delay across OFDM subcarriers.

Eq. (7) reveals that each propagation path contributes a separable outer-product structure across receive, transmit, and frequency modes. Consequently, the wideband channel tensor takes the form of a sum of rank-one components, yielding an intrinsic low-rank CP representation governed by the number of dominant paths [17, 23]. This physically grounded low-rank structure directly motivates tensor-based channel modeling and underpins the structure-informed estimation framework developed in Section 3.

3 Tensor Representations and Algebraic Priors

This section formalizes how fundamental propagation mechanisms in wideband MIMO channels manifest as intrinsic algebraic structure. It introduces CP and Tucker decompositions as principled parameterizations of this structure, providing physically interpretable and computationally efficient priors for pilot-limited channel estimation.

3.1 Canonical Polyadic Decomposition

The sparse multipath channel model in (7) admits a natural representation in terms of the CP decomposition [23],

$$\mathcal{H} = \sum_{r=1}^R \mathbf{u}_r \circ \mathbf{v}_r \circ \mathbf{w}_r, \quad (8)$$

where $\mathbf{u}_r \in \mathbb{C}^{N_r}$, $\mathbf{v}_r \in \mathbb{C}^{N_t}$, and $\mathbf{w}_r \in \mathbb{C}^{N_f}$ are factor vectors associated with the receive, transmit, and frequency modes, respectively, and R denotes the CP rank.

For channels with L dominant propagation paths, selecting $R = L$ yields a parsimonious and physically interpretable representation, with the correspondence

$$\mathbf{u}_\ell = \alpha_\ell \mathbf{a}_r(\theta_\ell), \quad \mathbf{v}_\ell = \mathbf{a}_t^*(\phi_\ell), \quad [\mathbf{w}_\ell]_k = e^{-j2\pi k\tau_\ell}, \quad (9)$$

where k indexes the subcarrier frequencies. Absorbing the complex gain α_ℓ into the receive-mode factor \mathbf{u}_ℓ is a matter of convention; the gain could equivalently enter \mathbf{v}_ℓ , \mathbf{w}_ℓ , or distribute across multiple factors. This scaling ambiguity is intrinsic to the CP decomposition: under the Kruskal uniqueness condition, the CP model is unique only up to permutation and scaling of its rank-one components [23].

This correspondence makes explicit that each rank-one tensor component represents a single physical propagation path, implying that the effective CP rank is governed by the number of dominant paths rather than the ambient channel dimensionality. As a result, CP is particularly well matched to propagation regimes dominated by specular ray-like components, such as millimeter-wave channels around 28 GHz, where a small number of strong paths typically captures most of the channel energy. This property underlies the effectiveness of CP-based models for sparse-channel and large-scale MIMO estimation [17]. The Kruskal uniqueness condition guarantees factor identifiability up to permutation and scaling, which suffices for reliable channel reconstruction. Extracting explicit physical parameters, such as angles of arrival or departure, from the estimated factors would require additional structural constraints—e.g., array calibration or explicit enforcement of Vandermonde structure—beyond the scope of this work, which focuses on CSI reconstruction rather than direct parameter estimation [16].

3.2 Tucker Decomposition

While CP enforces strict rank-one separability across all modes, the Tucker decomposition [24] provides a more flexible multilinear representation,

$$\mathcal{H} = \mathcal{G} \times_1 \mathbf{U}_r \times_2 \mathbf{U}_t \times_3 \mathbf{U}_f, \quad (10)$$

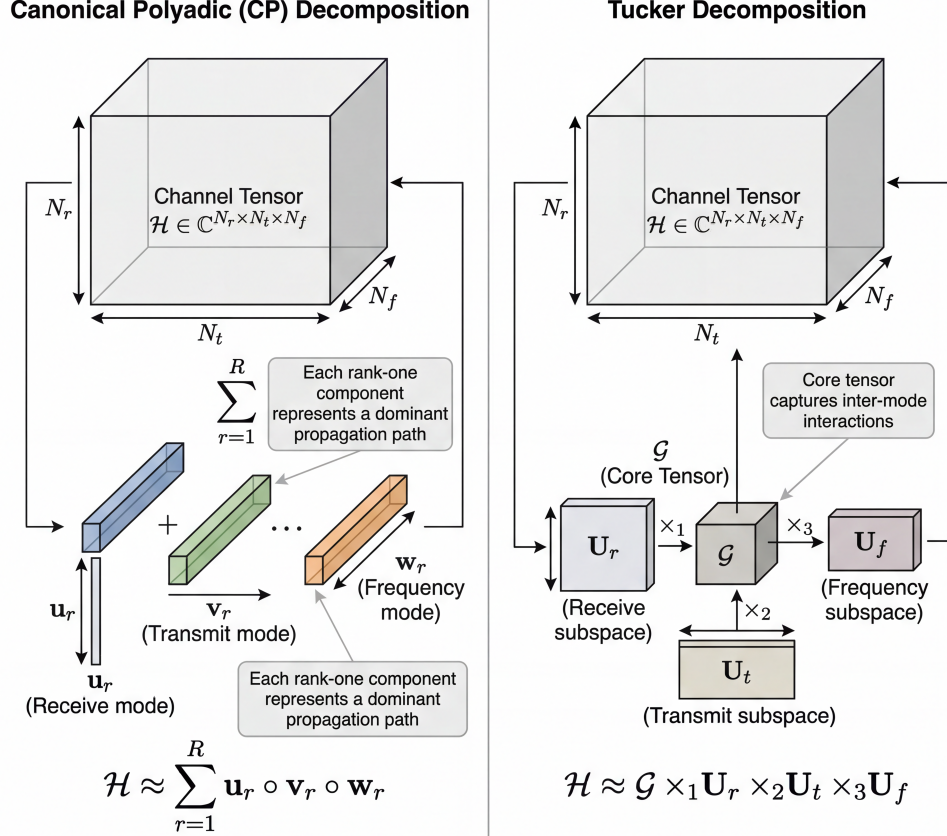


Figure 1: CP versus Tucker decompositions of the channel tensor $\mathcal{H} \in \mathbb{C}^{N_r \times N_t \times N_f}$. **Left:** CP expresses \mathcal{H} as a sum of R rank-one components ($\mathbf{u}_r \circ \mathbf{v}_r \circ \mathbf{w}_r$), enforcing strict mode separability. **Right:** Tucker factorizes \mathcal{H} into a core tensor \mathcal{G} and mode matrices ($\mathcal{G} \times_1 \mathbf{U}_r \times_2 \mathbf{U}_t \times_3 \mathbf{U}_f$), capturing inter-mode correlations.

where $\mathcal{G} \in \mathbb{C}^{R_r \times R_t \times R_f}$ is a low-dimensional core tensor capturing inter-mode coupling. The integers (R_r, R_t, R_f) denote the multilinear ranks of \mathcal{H} along the receive, transmit, and frequency modes, respectively. The factor matrices $\mathbf{U}_r \in \mathbb{C}^{N_r \times R_r}$, $\mathbf{U}_t \in \mathbb{C}^{N_t \times R_t}$, and $\mathbf{U}_f \in \mathbb{C}^{N_f \times R_f}$ contain orthonormal columns spanning the dominant subspaces associated with each mode.

Tucker generalizes CP, which the formulation recovers when the core tensor \mathcal{G} is superdiagonal with $R_r = R_t = R_f$, by relaxing strict separability across modes. The core tensor captures inter-mode interactions that independent rank-one components cannot express, enabling representation of richer spatial-spectral correlations. From a physical perspective, this flexibility allows Tucker models to capture clustered multipath and moderately diffuse scattering, where multiple rays share correlated angular and delay characteristics. The multilinear ranks (R_r, R_t, R_f) thus control a trade-off between compression and fidelity: smaller ranks yield stronger dimensionality reduction, while larger ranks enable finer modeling of scattering richness and model mismatch.

Fig. 1 illustrates the structural difference between CP and Tucker decompositions.

3.3 Algebraic Priors from Propagation Physics

The tensor decompositions introduced above encode algebraic properties that directly reflect the physical mechanisms governing channel formation:

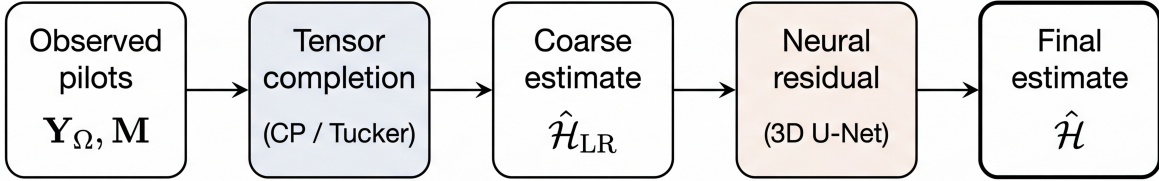


Figure 2: Tensor-NN framework: low-rank tensor completion produces a coarse estimate, refined by a 3D U-Net that learns residual components.

- **Low rank**, reflecting the presence of a limited number of dominant propagation paths;
- **Structured factor matrices**, capturing array-induced spatial correlations;
- **Frequency smoothness**, arising from finite delay spread and limited coherence bandwidth.

The literature has extensively exploited the low-rank property through matrix completion and matrix sensing formulations for mmWave and terahertz (THz) systems [25], complementing the tensor-based approach this paper adopts. Unlike geometric priors that rely on site-specific environmental descriptions or ray-tracing information, these algebraic constraints arise intrinsically from propagation physics and array structure, and therefore persist across diverse deployment scenarios. As a result, tensor representations provide robust, interpretable, and physically grounded priors for pilot-limited channel estimation, consistent with prior tensor-based formulations in wireless communications [17].

4 Structure-Informed Learning Framework

This section presents the proposed structure-informed learning framework for pilot-limited MIMO channel estimation. The framework combines algebraic priors induced by propagation physics with data-driven residual learning in a unified estimation pipeline. A low-rank tensor completion stage first enforces intrinsic multilinear structure arising from sparse multipath propagation, array geometry, and frequency coherence, yielding a physically consistent coarse channel estimate. A lightweight neural network then learns residual components that the idealized low-rank model does not capture, such as diffuse scattering effects, hardware non-idealities, and model mismatch. By decoupling structure enforcement from residual learning, the proposed approach achieves improved robustness and generalization in realistic pilot-limited regimes while retaining interpretability and computational efficiency. Fig. 2 illustrates the proposed two-stage estimation pipeline.

4.1 Problem Formulation

Given sparse pilot observations

$$\mathcal{Y}_\Omega = \mathcal{P}_\Omega(\mathcal{H} + \mathcal{N}) = \mathcal{P}_\Omega(\mathcal{H}) + \mathcal{P}_\Omega(\mathcal{N}), \quad (11)$$

the goal is to estimate the unknown channel tensor \mathcal{H} from incomplete and noisy measurements. This work poses the problem as

$$\begin{aligned} \hat{\mathcal{H}} &= \arg \min_{\mathcal{H}} \|\mathcal{P}_\Omega(\mathcal{H}) - \mathcal{Y}_\Omega\|_F^2 \\ \text{s.t. } \text{rank}_{\text{ml}}(\mathcal{H}) &= (R_r, R_t, R_f), \end{aligned} \quad (12)$$

where $\mathcal{P}_\Omega(\cdot)$ denotes projection onto the observed index set Ω , \mathcal{N} is i.i.d. complex Gaussian noise, and $\text{rank}_{\text{ml}}(\mathcal{H})$ denotes the multilinear rank of \mathcal{H} .

4.2 Tensor Completion via Alternating Projection

The alternating projection scheme enforces low-rank structure by iterating between: (i) projection onto a low-rank Tucker manifold via truncated HOSVD [24], and (ii) projection onto the data-consistency set defined by the observed pilot entries. This procedure alternates between structural regularization and measurement agreement.

While low-rank tensor models capture the dominant structure induced by sparse multipath propagation, practical channels exhibit deviations due to diffuse scattering, hardware impairments, and calibration inaccuracies. To account for these effects, the proposed framework augments algebraic tensor completion with a lightweight neural residual stage. The network learns structured residual components associated with model mismatch rather than performing generic denoising. This hybrid formulation follows a model-aided learning perspective in which algebraic structure provides the primary inductive bias and data-driven learning compensates non-idealities.

Algorithm 1 summarizes the Tucker completion procedure. Let \mathcal{Y} denote the observed tensor (zero-filled at unobserved entries) and $\mathcal{M} \in \{0, 1\}^{N_r \times N_t \times N_f}$ the sampling mask, where $[\mathcal{M}]_{ijk} = 1$ if $(i, j, k) \in \Omega$. The objective is to estimate $\hat{\mathcal{H}}$ with multilinear rank (R_r, R_t, R_f) consistent with the observations. Iterations terminate when $\delta^{(t)} < \epsilon$ or $t = T$; unless otherwise stated, $\epsilon = 10^{-6}$ and $T = 20$. In all tested configurations, convergence was empirically observed within 10–15 iterations, confirming that $T = 20$ provides sufficient margin without introducing unnecessary computation. The tolerance $\epsilon = 10^{-6}$ ensures that residual changes on the observed entries are negligible relative to the pilot-set norm, and was verified to be neither too tight nor too loose across the SNR and pilot-density ranges of all experiments.

Alternating projection defines a non-convex feasibility procedure that typically converges to a stationary point under standard regularity conditions [26], without guarantees of global optimality; CP-based formulations exhibit analogous behavior. The framework assumes the multilinear ranks (R_r, R_t, R_f) (Tucker) and the CP rank R known or selected a priori. In practice, rank selection may rely on information criteria (e.g., Akaike Information Criterion (AIC)) or singular-value inspection of tensor unfoldings [23]. Synthetic experiments match ranks to the number of propagation paths ($L = 5$), whereas DeepMIMO ranks receive conservative choices based on representative singular-value decay. Underestimated ranks increase the residual $\Delta\mathcal{H} = \mathcal{H} - \mathcal{H}_{\text{LR}}$, motivating the neural residual stage (subsection 5.4).

The Tucker stage performs reconstruction via alternating projections, iterating truncated higher-order singular value decomposition (HOSVD) on the current estimate followed by enforcement of consistency on the observed entries (Algorithm 1). The CP stage performs reconstruction via missing-data-aware weighted alternating least squares (CP-WALS), minimizing a weighted Frobenius norm over the observed entries only. The implementation optionally supports multiple random restarts, selecting the best solution by observed-data fit (NMSE on the pilot set) to reduce initialization sensitivity; when only one restart is used, this selection step is degenerate. Tucker alternating projections maintain a dense iterate and enforce data consistency on the observed set at each iteration, rather than optimizing exclusively on the sparse observation set. In the hybrid Tensor-NN pipeline, the low-rank reconstruction runs first and its output serves as the input prior for neural residual correction.

4.3 Computational Complexity

For CP decomposition with rank R , the number of parameters scales as $\mathcal{O}(R(N_r + N_t + N_f))$, compared with $\mathcal{O}(N_r N_t N_f)$ for unstructured estimation [23]. For typical dimensions ($N_r = N_t = 32$, $N_f = 128$, $R = 5$), this corresponds to approximately $136\times$ reduction in degrees of freedom. This substantial complexity reduction explains the effectiveness and scalability of structure-informed estimation in pilot-limited MIMO systems, consistent with prior observations [17].

Algorithm 1 Tucker Completion via Alternating Projection

Input: Observed tensor \mathcal{Y} , mask \mathcal{M} , ranks (R_r, R_t, R_f) , max iterations T , tolerance ϵ

Output: Completed tensor $\hat{\mathcal{H}}$

```
 $\mathcal{X}^{(0)} \leftarrow \mathcal{Y}$   
for  $t = 1, \dots, T$  do  
   $\hat{\mathcal{X}} \leftarrow \text{HOSVD}_{\text{trunc}}(\mathcal{X}^{(t-1)}, R_r, R_t, R_f)$   
   $\mathcal{X} \leftarrow \mathcal{M} \odot \mathcal{Y} + (1 - \mathcal{M}) \odot \hat{\mathcal{X}}$   
   $\delta^{(t)} \leftarrow \frac{\|(\mathcal{X} - \mathcal{X}^{(t-1)}) \odot \mathcal{M}\|_F}{\|\mathcal{Y} \odot \mathcal{M}\|_F + \epsilon}$   
  if  $\delta^{(t)} < \epsilon$  then  
    break  
  end if  
   $\mathcal{X}^{(t)} \leftarrow \hat{\mathcal{X}}$   
end for  
return  $\hat{\mathcal{H}} \leftarrow \hat{\mathcal{X}}$ 
```

4.4 Hybrid Tensor–Neural Extension

Although tensor decompositions capture dominant low-dimensional structure induced by sparse multipath propagation, residual errors arise from diffuse scattering, hardware impairments, or model mismatch. To account for these effects, the channel takes the form

$$\mathcal{H} = \mathcal{T}(\boldsymbol{\theta}) + \Delta\mathcal{H}_{\text{NN}}(\phi), \quad (13)$$

where $\mathcal{T}(\boldsymbol{\theta})$ denotes a low-rank tensor component and $\Delta\mathcal{H}_{\text{NN}}(\phi)$ a lightweight neural residual. This decomposition restricts learning to a correction term rather than the full channel, reducing sample complexity, mitigating overfitting, and improving generalization.

Estimation proceeds in two stages. First, the framework obtains the structured component $\mathcal{T}(\boldsymbol{\theta})$ by solving the rank-constrained problem (12) via truncated HOSVD with alternating projections for Tucker. Second, the neural network learns the residual by minimizing the supervised mean-squared error (MSE) between predicted and true residuals,

$$\mathcal{L}_{\text{NN}}(\phi) = \|\Delta\mathcal{H}_{\text{NN}}(\phi) - (\mathcal{H} - \mathcal{H}_{\text{LR}})\|_F^2, \quad (14)$$

where \mathcal{H}_{LR} is the low-rank reconstruction and \mathcal{H} the ground-truth channel. This two-stage approach aligns with model-driven and algorithm-unrolling paradigms in signal processing [27–29]. The two stages are trained sequentially: the tensor completion stage is executed first and its output \mathcal{H}_{LR} is treated as fixed during neural network training, with no gradient propagation through the tensor stage.

4.4.1 Neural Architecture and Training

The residual term $\Delta\mathcal{H}_{\text{NN}}$ takes the form of a lightweight three-dimensional U-Net architecture [30], denoted **Residual3DUNet**. U-Net offers a strong inductive bias in reconstruction tasks, combining multiscale context aggregation with skip connections that preserve fine structural information. This design suits the learning of systematic residual components arising from model mismatch rather than generic denoising. The 3D formulation operates directly on the spatial–frequency tensor, enabling joint modeling of antenna and subcarrier correlations. A lightweight configuration limits parameter count and keeps the tensor model as the primary structural prior. Table 1 and Fig. 3 detail the architecture.

The input consists of the observed tensor \mathcal{Y}_Ω represented by separate real and imaginary channels, yielding $C_{\text{in}} = 2$ input channels, optionally augmented with a binary pilot mask ($C_{\text{in}} = 3$). The architecture

Table 1: Residual3DUNet architecture for neural residual learning.

Stage	Operation	Channels
Input	—	C_{in}
Encoder-1	Conv3D + ReLU ($3^3/1$)	$C_{\text{in}} \rightarrow C$
	Conv3D + ReLU ($3^3/1$)	$C \rightarrow C$
Downsample	Conv3D ($2^3/2$)	$C \rightarrow 2C$
Encoder-2	ReLU \rightarrow Conv3D \rightarrow ReLU ($3^3/1$)	$2C \rightarrow 2C$
Upsample	ConvTranspose3D ($2^3/2$)	$2C \rightarrow C$
Decoder-1	Concat + ReLU \rightarrow Conv3D + ReLU ($3^3/1$)	$2C \rightarrow C$
Output	Conv3D ($3^3/1$)	$C \rightarrow C_{\text{in}}$

Notation: k^3/s denotes kernel size $k \times k \times k$ with stride s . Base width $C = 16$.

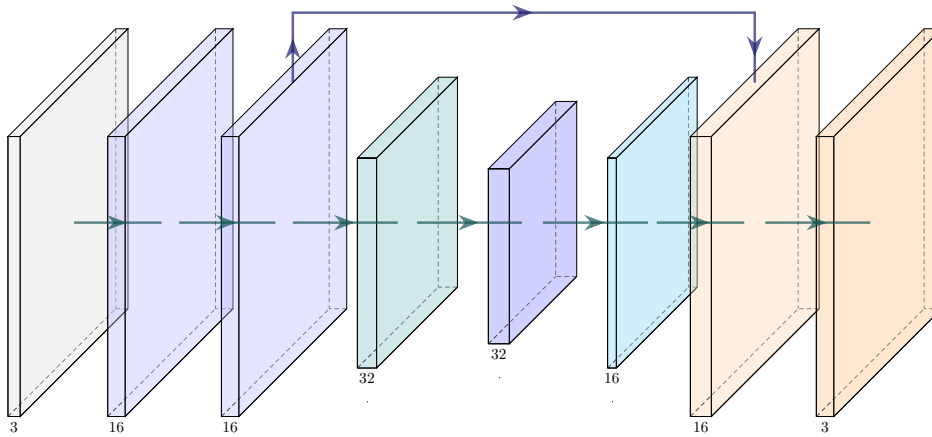


Figure 3: **Residual3DUNet architecture** ($C_{\text{in}} \in \{2, 3\}$, base width $C = 16$). Encoder-1 applies two Conv3D+ReLU ($3^3/1$) layers followed by Conv3D ($2^3/2$) downsampling ($C \rightarrow 2C$). Encoder-2 keeps $2C \rightarrow 2C$ at the bottleneck. The decoder upsamples via ConvTranspose3D ($2^3/2$), concatenates encoder skip features, and maps $2C \rightarrow C$. A final Conv3D ($3^3/1$) projects $C \rightarrow C_{\text{in}}$, yielding $\Delta \mathcal{H}_{\text{NN}}$.

employs a single encoder–decoder level. The base channel width C equals 16 in all experiments unless otherwise stated.

The encoder applies two $3 \times 3 \times 3$ convolutional layers with padding 1, each followed by ReLU activation, and performs downsampling via a $2 \times 2 \times 2$ strided convolution doubling the channel dimension. The second encoder block begins with ReLU, followed by a $3 \times 3 \times 3$ convolution and another ReLU. The decoder mirrors this structure using transposed convolution for upsampling, concatenation with corresponding encoder features through a skip connection, and two $3 \times 3 \times 3$ convolutions with ReLU activations. The final layer projects features back to the input channel dimension, producing the residual estimate $\widehat{\mathcal{R}}$. When necessary, trilinear interpolation aligns tensor dimensions prior to skip-connection concatenation. The architecture employs no batch normalization, dropout, or other explicit regularization layers.

The framework obtains the reconstructed channel as

$$\widehat{\mathcal{H}} = \mathcal{H}_{\text{LR}} + \widehat{\mathcal{R}}, \quad (15)$$

where \mathcal{H}_{LR} denotes the low-rank tensor approximation. The resulting network contains approximately 50k

trainable parameters.

Training details Training uses the Adam optimizer [31] with fixed learning rate 10^{-3} and batch size 2 (unless otherwise stated). The procedure uses no learning-rate decay or warm-up. It applies early stopping only to the ResNet baseline, leaving it disabled by default; the hybrid Tensor-NN trains for a fixed number of epochs. The implementation initializes network weights using PyTorch default schemes, corresponding to Kaiming/He uniform initialization for convolutional and transposed convolutional layers, with biases set to zero when present [32].

The training procedure applies no explicit data augmentation. Random channel generation provides training variability, supplemented when enabled by sampling pilot ratios and SNR values over predefined ranges (multi-pilot and multi-SNR training). The hybrid Tensor-NN trains for a fixed number of epochs without early stopping.

4.4.2 Residual Structure and Architectural Rationale

After low-rank tensor reconstruction, the residual $\Delta\mathcal{H} = \mathcal{H} - \mathcal{H}_{\text{LR}}$ exhibits two dominant characteristics: (i) spatial and spectral smoothness induced by bandlimited propagation and finite delay spread, and (ii) localized components arising from diffuse scattering, hardware impairments, and rank mismatch. This structure naturally spans multiple spatial and frequency scales.

The U-Net architecture matches this residual structure well: its encoder captures coarse global context through progressive downsampling, while skip connections preserve fine-scale localized information. This design enables efficient reconstruction of multi-scale residual patterns with a small parameter budget, a property proven effective in inverse problems and denoising tasks involving structured residuals.

5 Simulation Results

This section evaluates pilot-limited wideband MIMO channel estimation under synthetic and ray-tracing-based propagation models through four experiments. Experiment 1 benchmarks Tucker completion against LS, LMMSE, and OMP baselines across pilot densities under a controlled synthetic channel at fixed SNR. Experiment 2 isolates the performance gap between CP and Tucker decompositions as a function of SNR under the synthetic specular channel model. Experiment 3 validates the hybrid Tensor-NN framework on DeepMIMO ray-tracing data, assessing generalization beyond the synthetic model. Experiment 4 characterizes sample complexity by empirically mapping recovery thresholds in the (L, ρ) plane. Across all scenarios, the goal is to quantify how intrinsic tensor structure—in particular, low multilinear rank induced by sparse scattering—enables reliable reconstruction of the wideband channel tensor \mathcal{H} from noisy and incomplete pilot observations.

5.1 Setup

For synthetic experiments, the setup represents the wideband channel as a third-order tensor $\mathcal{H} \in \mathbb{C}^{N_r \times N_t \times N_f}$ with $N_r = N_t = 32$ antennas and $N_f = 128$ subcarriers, generating it according to the multipath model in (7) with L dominant paths. Angles satisfy $\theta_\ell, \phi_\ell \sim \mathcal{U}[-\pi/2, \pi/2]$ (angular spread 180°), complex gains α_ℓ are drawn i.i.d. from $\mathcal{CN}(0, 1)$ and normalized to unit total power, and normalized delays satisfy $\tau_\ell \sim \mathcal{U}[0, 1)$. ULA with half-wavelength spacing serve at both ends [2, 7]. The setup models pilot acquisition as entry-wise random sampling over an index set Ω with pilot ratio $\rho = |\Omega|/(N_r N_t N_f)$ [26, 33]. The model applies AWGN only to observed entries. The noise variance is set according to a global SNR

Table 2: Simulation parameters. Exp. 4 employs 100 Monte Carlo realizations, as its objective is recovery-threshold (sample-complexity) characterization rather than statistical performance averaging.

Parameter	Exp. 1	Exp. 2	Exp. 3	Exp. 4
Sweep variable	Pilot ratio	SNR	Pilot ratio	Pilot ratio / L paths
Pilot ratio	2–20%	8%	2–20%	1–25%
SNR (dB)	10	–5 to 20	10	10
L paths	5	5	5	{2, 3, 5, 8, 10, 15}
$N_r \times N_t \times N_f$	$32 \times 32 \times 128$	$32 \times 32 \times 128$	$16 \times 32 \times 64$	$32 \times 32 \times 128$
Tucker ranks	(4, 4, 6)	(5, 5, 6)	(4, 4, 8)	($L, L, L + 1$)
CP rank R	—	5	5	—
Dataset	Synthetic	Synthetic	DeepMIMO	Synthetic
MC runs	500	500	500	100

reference,

$$\sigma_n^2 = \frac{\|\mathcal{H}\|_F^2 / (N_r N_t N_f)}{10^{\text{SNR}/10}}, \quad (16)$$

where $\|\mathcal{H}\|_F^2 / (N_r N_t N_f)$ denotes the average power per channel coefficient over the full tensor, independent of the pilot set Ω and pilot ratio ρ . This definition is applied identically across all experiments, including the DeepMIMO scenario (Experiment 3), ensuring strict SNR comparability across pilot densities.

For synthetic experiments, the channel model operates in a normalized discrete-frequency domain, where delays are specified in sample units, leaving bandwidth undefined. Since the evaluation targets reconstruction accuracy rather than physical delay interpretation, results remain invariant to bandwidth scaling.

The following estimators enter the comparison:

- **LS**: baseline estimator setting unobserved entries to zero;
- **LMMSE**: linear MMSE estimator with covariance estimated from channel samples, used as a practical statistical reference baseline;
- **orthogonal matching pursuit (OMP)**: joint sparse recovery using simultaneous OMP (SOMP) with shared support across subcarriers and a Kronecker ULA steering dictionary (Rx/Tx). For notation consistency, this joint SOMP curve carries the label “OMP” in the plots [7];
- **Tucker**: completion via alternating projection between truncated HOSVD with multilinear ranks (R_r, R_t, R_f) and data-consistency enforcement on Ω [24, 26];
- **CP**: rank- R CP completion with missing-data-aware WALS, selecting the best restart by observed-data fit [23];
- **Tensor-NN**: proposed hybrid architecture combining low-rank tensor completion and a lightweight 3D U-Net for residual learning.

The experiments measure performance by normalized mean-squared error (NMSE),

$$\text{NMSE} = \frac{\|\hat{\mathcal{H}} - \mathcal{H}\|_F^2}{\|\mathcal{H}\|_F^2}, \quad (17)$$

averaging each result over Monte Carlo (MC) realizations. Table 2 summarizes experiment settings.

Experiment 1 uses ranks (4, 4, 6) to assess robustness under mild rank underestimation; Experiment 2 uses (5, 5, 6) to match the channel rank more closely and isolate the CP–Tucker comparison at higher SNR.

This work also evaluates realistic propagation conditions using ray-tracing-based channels from the DeepMIMO dataset [34]. The experiments adopt the ASU_Campus_3p5 scenario (DeepMIMO v4 pre-release), generated with Remcom Wireless InSite at 3.5 GHz.

Experiment 3 employs ULA with $N_r = 16$ receive antennas and $N_t = 32$ transmit antennas, and OFDM with $N_f = 64$ subcarriers over 50 MHz bandwidth, yielding $\mathcal{H} \in \mathbb{C}^{16 \times 32 \times 64}$ (Table 2). The study uses channels without path truncation and normalizes them to unit average power; low-rank structure therefore emerges empirically. The protocol forms training and test sets via random subsampling of user locations with fixed seeds for reproducibility. The partitioning enforces no explicit geographic separation; strict spatial generalization remains future work. Channels are normalized to unit average power prior to noise addition, so that $\|\mathcal{H}\|_F^2 / (N_r N_t N_f) = 1$ and the noise variance reduces to $\sigma_n^2 = 10^{-\text{SNR}/10}$, consistently with the global SNR definition in (16).

Experiment 4 adopts the same synthetic channel model with $N_r = N_t = 32$ and $N_f = 128$, varying the number of paths $L \in \{2, 3, 5, 8, 10, 15\}$ and sweeping pilot ratios from 1% to 25% across 14 sample points, with Tucker ranks set to $(L, L, L + 1)$. Each result averages over 100 Monte Carlo realizations, and the analysis defines successful recovery as $\text{NMSE} \leq 10^{-2}$.

5.2 Experiment 1: Tensor Completion under Pilot Scarcity

Fig. 4 shows NMSE as a function of pilot ratio at $\text{SNR} = 10$ dB with $L = 5$ paths (500 MC runs, global-SNR setting). This experiment highlights the benefit of Tucker tensor completion under pilot undersampling. CP is excluded from this comparison as its performance relative to Tucker under the synthetic specular channel model is isolated in Experiment 2 (Section 5.3), which sweeps SNR at fixed pilot ratio and provides a cleaner characterization of the CP–Tucker trade-off; furthermore, CP exhibits heavy-tail divergence at low pilot densities (as confirmed in Experiment 3), which would compress the vertical scale and obscure the Tucker–baseline comparison that is the focus of this experiment.

LS remains weak across the sweep, ranging from approximately -0.08 dB at $\rho = 2\%$ to -0.86 dB at $\rho = 20\%$, confirming that naive interpolation cannot recover channel structure from sparse pilots. LMMSE provides only modest improvement, decreasing from about -0.16 dB to -1.28 dB over the same range. OMP improves over LS/LMMSE and reaches around -3.5 dB at higher pilot ratios, but still exhibits a clear performance floor.

Tucker completion improves monotonically with pilot density, from about -1.80 dB at $\rho = 2\%$ to -12.79 dB at $\rho = 20\%$. At $\rho = 10\%$, Tucker achieves $\text{NMSE} \approx -11.25$ dB, corresponding to gains of 10.88 dB over LS (≈ -0.37 dB), 10.52 dB over LMMSE, and 7.83 dB over OMP (≈ -3.42 dB). Notably, at the most extreme sparsity point ($\rho = 2\%$), OMP is slightly better than Tucker (about 0.67 dB), but Tucker becomes clearly dominant from $\rho \geq 4\%$ onward.

5.3 Experiment 2: CP versus Tucker Decomposition

Fig. 5 compares Tucker and CP as a function of SNR at $\rho = 8\%$. This experiment addresses decomposition choice under the synthetic specular channel model.

Both tensor methods outperform LS and LMMSE across the full SNR range, and CP consistently outperforms Tucker. At low SNR (-5 dB), CP already provides a slight gain over Tucker (CP ≈ -1.82 dB versus Tucker ≈ -1.37 dB, about 0.45 dB). The gap widens markedly with SNR: at 20 dB, CP reaches $\text{NMSE} \approx -25.00$ dB versus Tucker ≈ -11.89 dB, i.e., about 13.11 dB advantage. Compared to OMP, Tucker is slightly worse at -5 dB (OMP ≈ -2.09 dB) but becomes clearly better from 0 dB onward.

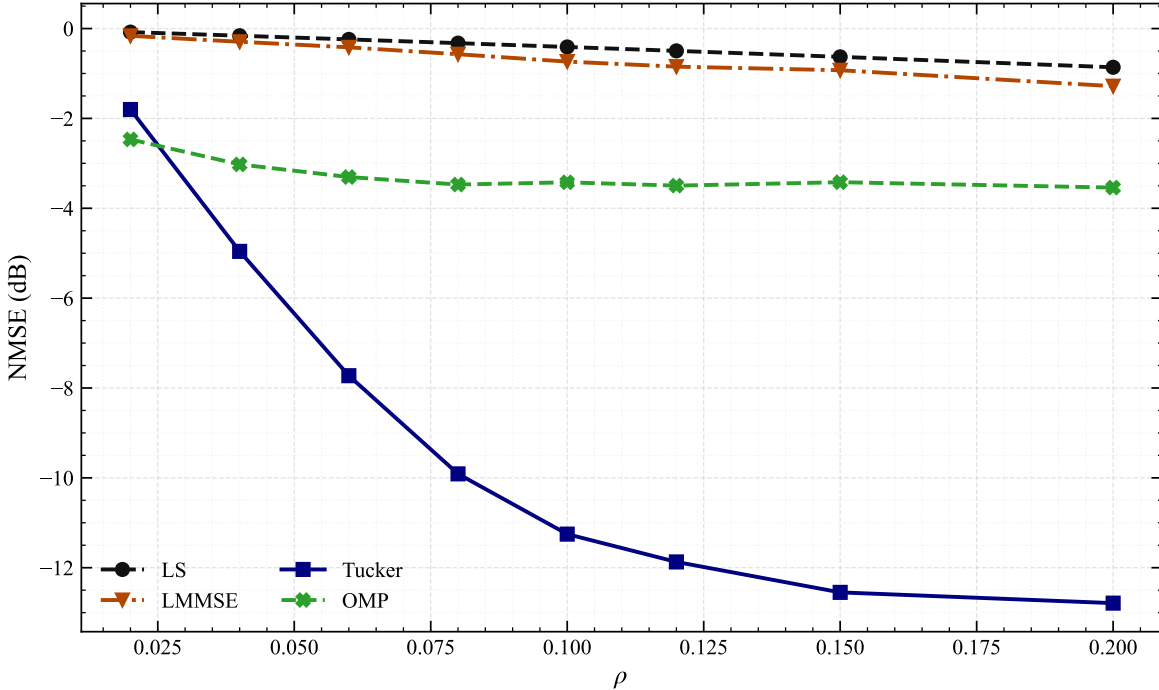


Figure 4: NMSE versus pilot ratio for synthetic specular channels (SNR = 10 dB, $L = 5$, Tucker ranks (4, 4, 6), 500 MC runs).

This behavior is consistent with the synthetic model in (7), where the channel consists of a small number of rank-one components. In this regime, CP provides a tighter representation than Tucker’s full-core parameterization.

5.4 Experiment 3: Hybrid Tensor–Neural Estimation on DeepMIMO

Fig. 6 evaluates the complete framework on ray-tracing-based DeepMIMO channels at SNR = 10 dB. These channels exhibit higher effective rank and stronger model mismatch relative to the idealized synthetic setting.

The comparison includes LS, LMMSE, OMP, Tucker, CP, Tensor-NN, and a purely data-driven ResNet baseline. Tensor-NN achieves the best overall performance across all pilot ratios, with NMSE decreasing from approximately -4.56 dB at $\rho = 2\%$ to approximately -18.43 dB at $\rho = 20\%$.

At $\rho = 8\%$, Tensor-NN reaches approximately -13.72 dB, improving by about 2.26 dB over CP (≈ -11.46 dB), 4.80 dB over Tucker (≈ -8.93 dB), and 5.85 dB over LMMSE (≈ -7.87 dB). At $\rho = 20\%$, Tensor-NN remains best (≈ -18.43 dB), with a positive margin over CP (≈ -17.43 dB, about 1.00 dB advantage).

CP shows severe instability at extreme pilot scarcity ($\rho = 2\%$), with heavy-tailed outliers in Monte Carlo runs: its mean NMSE becomes strongly degraded (about $+13.96$ dB), consistent with rare divergent cases dominating the average.

Comparison with the ResNet baseline A purely data-driven ResNet baseline [35–37] is included to quantify the contribution of tensor structural priors over unconstrained deep learning. The ResNet is a 3D architecture operating on the real and imaginary parts of the observation and the pilot mask (3-channel input), with a $3 \times 3 \times 3$ Conv3D stem followed by 4 residual blocks (each comprising two $3 \times 3 \times 3$ Conv3D layers

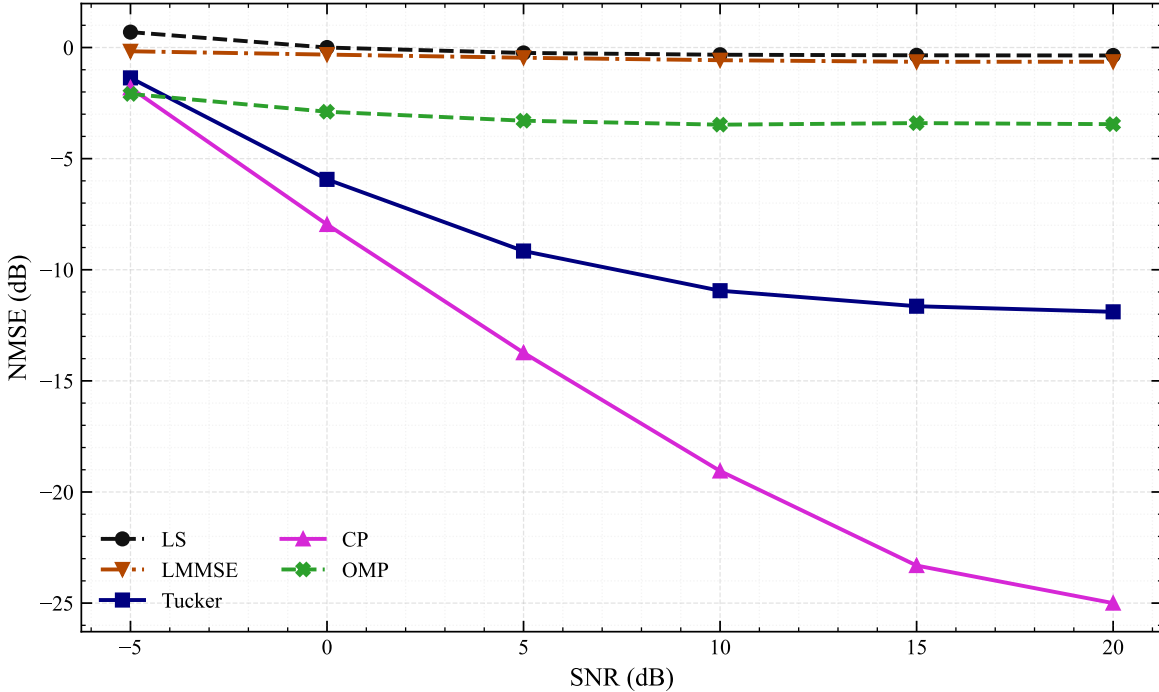


Figure 5: NMSE versus SNR for synthetic specular channels ($\rho = 8\%$, $L = 5$, Tucker ranks $(5, 5, 6)$, CP rank $R = 5$, 500 MC runs).

with ReLU activations) and a final $3 \times 3 \times 3$ Conv3D predicting the 2-channel complex output (base channels = 32). Training uses paired $(\mathcal{H}, \mathcal{Y}_\Omega)$ samples optimized with Adam under multi-SNR and multi-pilot regimes, with pilot-consistency weight $\lambda_{\text{pilot}} = 0.1$.

Tensor-NN outperforms ResNet at all pilot ratios: by 1.53 dB at $\rho = 2\%$, 3.64 dB at $\rho = 4\%$, 3.58 dB at $\rho = 6\%$, 3.67 dB at $\rho = 8\%$, 3.91 dB at $\rho = 10\%$, 4.91 dB at $\rho = 15\%$, and 5.67 dB at $\rho = 20\%$.

Overall, the hybrid Tensor-NN framework provides the most robust reconstruction across the full pilot-density range, combining the structural efficiency of tensor decomposition with the flexibility of neural residual correction under realistic DeepMIMO propagation conditions.

5.5 Experiment 4: Sample Complexity Analysis

This experiment empirically characterizes the sample complexity of tensor completion by determining the recovery threshold of Tucker reconstruction as a function of the number of observed entries $|\Omega|$. The setup generates synthetic channels according to the model in Section 5.1, with $N_r = N_t = 32$ antennas, $N_f = 128$ subcarriers, and $L \in \{2, 3, 5, 8, 10, 15\}$ propagation paths. The sweep covers pilot ratios from 1% to 25% across 14 sample points, with finer spacing at low pilot ratios (and consequently finer resolution near the transition region). Each result averages over 100 Monte Carlo realizations, and the analysis defines successful recovery as $\text{NMSE} \leq 10^{-2}$, which determines the empirical threshold $|\Omega|_{\text{min}}$. Following the implementation, the experiments adapt Tucker ranks to L via $(R_r, R_t, R_f) = (L, L, L+1)$ (capped by N_f).

Recovery curves Fig. 7 plots NMSE versus pilot ratio ρ for each value of L at $\text{SNR} \in \{10, 20, 30\}$ dB. Two consistent trends emerge. First, the recovery transition shifts toward higher pilot densities as L increases, reflecting the growing intrinsic dimensionality of the channel model. Second, higher SNR sharpens the transition and lowers NMSE once the recovery region is reached. At $\text{SNR} = 10$ dB, no configuration

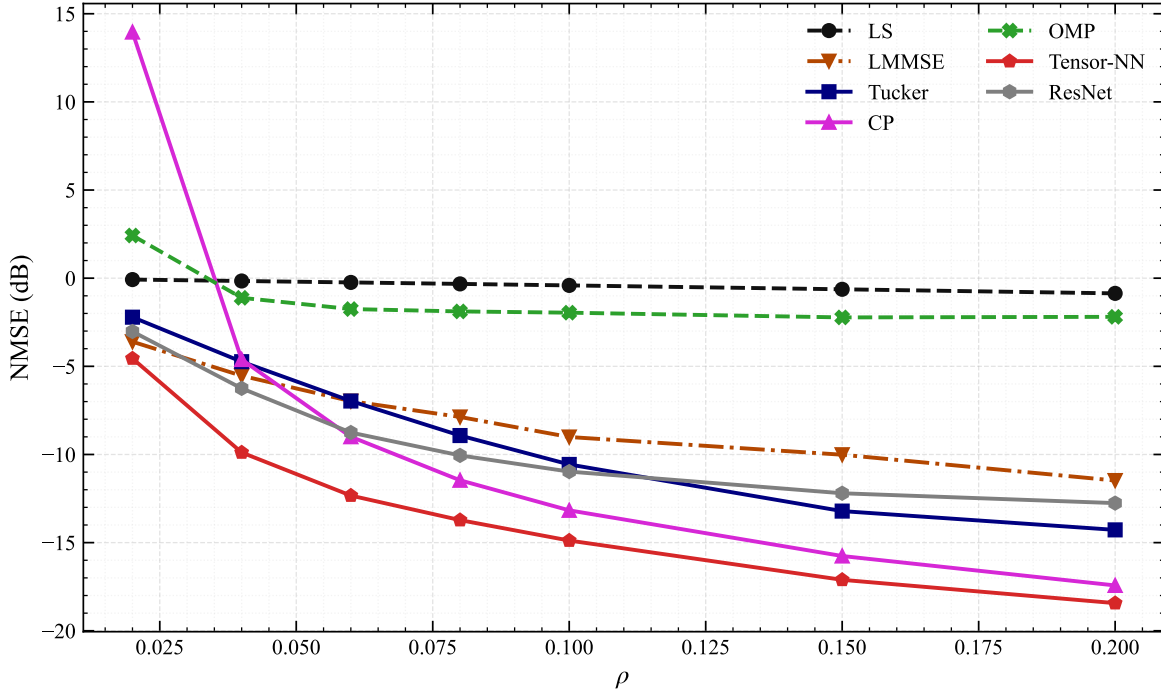


Figure 6: NMSE versus pilot ratio (DeepMIMO ASU_Campus_3p5, SNR = 10 dB, 500 MC runs).

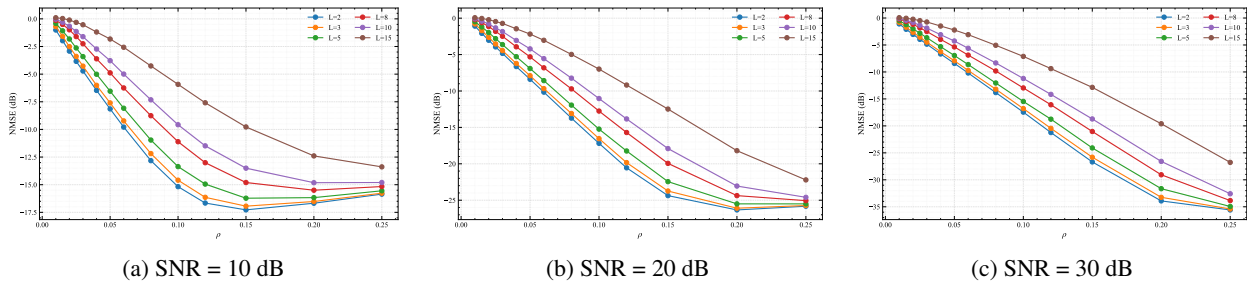


Figure 7: Recovery curves showing NMSE versus pilot ratio ρ for varying number of paths L . Higher SNR sharpens the transition and lowers NMSE within the feasible region.

achieves $\text{NMSE} \leq 10^{-2}$ within the tested 25% pilot range, indicating a noise-limited regime where increasing pilot density alone cannot compensate for measurement noise. The curves remain monotonic but exhibit no clear threshold within the tested range.

Recovery region heatmaps Fig. 8 visualizes the recovery region in the (L, ρ) plane. The transition band between successful recovery and failure shifts to higher pilot densities as L increases, consistent with the growth in intrinsic model complexity. At SNR = 10 dB, no configuration reaches the $\text{NMSE} \leq 10^{-2}$ threshold within the tested range, indicating a noise-limited regime. For SNR $\in \{20, 30\}$ dB, the empirical thresholds lie in the 12–25% pilot range and increase monotonically with L . The difference between 20 and 30 dB is modest (with only small reductions of ρ_{\min} for some L), indicating that L dominates the feasibility boundary while higher SNR mainly sharpens the transition and lowers NMSE within the feasible region. These heatmaps provide a compact visualization of the feasibility region for reliable channel reconstruction.

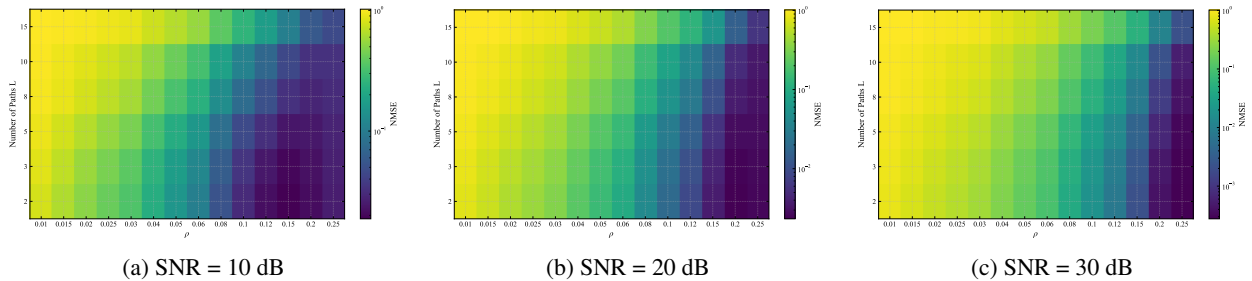


Figure 8: Recovery region heatmaps over (L, ρ) .

Table 3: Empirical thresholds for $\text{NMSE} \leq 10^{-2}$ and oversampling factor.

SNR (dB)	L	ρ_{\min}	$ \Omega _{\min}$	C
20	2	0.120	15,729	40.96
20	3	0.150	19,661	34.13
20	5	0.150	19,661	20.48
20	8	0.200	26,214	17.07
20	10	0.200	26,214	13.65
20	15	0.250	32,768	11.38
30	2	0.120	15,729	40.96
30	3	0.120	15,729	27.31
30	5	0.150	19,661	20.48
30	8	0.150	19,661	12.80
30	10	0.200	26,214	13.65
30	15	0.250	32,768	11.38

Empirical thresholds and oversampling factor Table 3 reports the minimum pilot ratio ρ_{\min} and corresponding observation count $|\Omega|_{\min}$ required to achieve $\text{NMSE} \leq 10^{-2}$. At SNR = 10 dB, no configuration reaches this threshold within the tested pilot range. For SNR $\in \{20, 30\}$ dB, the thresholds fall within the 12–25% pilot interval and exhibit an overall increasing trend with L , indicating that sample complexity is primarily governed by intrinsic channel structure rather than noise level.

To interpret these results, this article compares them against the heuristic degrees-of-freedom scaling commonly used in low-rank tensor recovery:

$$|\Omega|_{\min} \approx C L (N_r + N_t + N_f), \quad (18)$$

where C denotes an oversampling factor capturing deviations from the idealized identifiability limit. This expression is CP-inspired: it counts L factor vectors of lengths N_r , N_t , and N_f , totalling $L(N_r + N_t + N_f)$ free parameters.

For Tucker decompositions with multilinear ranks (R_r, R_t, R_f) , the effective degrees of freedom are

$$d_{\text{Tucker}} = R_r R_t R_f + R_r N_r + R_t N_t + R_f N_f, \quad (19)$$

comprising the core tensor ($R_r R_t R_f$ entries) and the three factor matrices ($R_n N_n$ entries each). For the ranks $(R_r, R_t, R_f) = (L, L, L + 1)$ used in Experiment 4, (19) yields values ranging from $d_{\text{Tucker}} = 524$ at $L = 2$ to $d_{\text{Tucker}} = 6608$ at $L = 15$, compared with $L(N_r + N_t + N_f) \in \{384, 2880\}$ from (18). The ratio

$d_{\text{Tucker}}/[L(N_r + N_t + N_f)]$ grows from ≈ 1.36 at $L = 2$ to ≈ 2.29 at $L = 15$, reflecting the cubic growth of the core-tensor term $R_r R_t R_f \sim L^3$ relative to the linear scaling of the CP heuristic.

The rightmost column of Table 3 lists the empirically observed values of C . The measured range ($C \approx 11\text{--}41$) exceeds theoretical minima established for incoherent low-rank tensors under noiseless and asymptotic conditions [38]. Several practical factors contribute to this gap. First, the CP-inspired reference (18) increasingly underestimates true Tucker complexity as L grows, since it does not account for the core-tensor degrees of freedom in (19); the empirical C must therefore absorb this structural gap in addition to other sources of inefficiency. Second, finite-sample effects and interpolation in threshold estimation introduce bias. Third, practical convergence limitations of the alternating projection algorithm under noisy and sparse observations may prevent attainment of the optimal recovery boundary.

Nonetheless, the empirical evidence indicates that the minimum observation count scales predominantly with intrinsic channel complexity—characterized by the number of dominant propagation paths and effective subspace dimensions—rather than with the ambient tensor size $N_r N_t N_f$, consistent with Table 3.

Key findings The results confirm the existence of a sharp recovery threshold and yield three principal insights:

1. Successful tensor completion requires a number of observations that scales with intrinsic model complexity rather than ambient tensor dimension.
2. The effective oversampling factor C depends on the decomposition type, SNR, and algorithmic efficiency.
3. At moderate SNR (≥ 20 dB), reliable recovery is achievable with 12–25% pilot density for channels with up to 15 dominant propagation paths.

5.6 Discussion

The experimental results yield five main findings:

1. **Tensor completion mitigates pilot scarcity.** Fig. 4 shows that Tucker completion yields substantial NMSE gains over LS, LMMSE, and OMP across all pilot ratios. At $\rho = 10\%$, Tucker achieves $\text{NMSE} \approx -11.25$ dB, corresponding to gains of 10.88 dB over LS (≈ -0.37 dB) and 7.83 dB over OMP (≈ -3.42 dB). LS remains below -1 dB across the full sweep, confirming that naive zero-filling cannot recover channel structure under sparse sampling. OMP improves over LS and LMMSE but still exhibits a performance floor around -3.5 dB due to dictionary mismatch and pilot scarcity. Notably, at the most extreme sparsity point ($\rho = 2\%$), OMP is slightly better than Tucker by about 0.67 dB, but Tucker becomes clearly dominant from $\rho \geq 4\%$ onward.
2. **Decomposition performance depends on channel structure.** Fig. 5 indicates that CP and Tucker perform similarly at low SNR (-5 dB: CP ≈ -1.82 dB versus Tucker ≈ -1.37 dB, about 0.45 dB difference), but CP is consistently better across the full SNR range under the synthetic specular model. The CP advantage increases with SNR and reaches 13.11 dB at SNR = 20 dB (CP ≈ -25.00 dB versus Tucker ≈ -11.89 dB), consistent with the specular multipath structure of (7), where each propagation path contributes a rank-one component that matches the CP parameterization exactly.

Importantly, CP maintains its advantage over Tucker even under the realistic DeepMIMO conditions of Experiment 3: for $\rho \geq 6\%$, CP outperforms Tucker by approximately 1–2 dB across the pilot range. The exception occurs at extreme pilot scarcity ($\rho = 2\%$), where CP exhibits heavy-tail divergence (mean NMSE $\approx +13.96$ dB) due to numerical instability of the WALS algorithm under severe

undersampling, while Tucker’s alternating-projection scheme remains stable. This contrast highlights a key practical trade-off: CP offers superior reconstruction accuracy whenever sufficient pilots are available, but Tucker provides a safer fallback at the extreme undersampling boundary where CP initialization is unreliable. The hybrid Tensor–NN framework, which builds on Tucker completion, inherits this numerical stability while recovering performance through neural residual correction.

3. **Hybrid Tensor–NN improves robustness on realistic channels.** Fig. 6 (DeepMIMO, SNR = 10 dB) shows Tensor-NN as the best overall method across all pilot ratios. At $\rho = 8\%$, Tensor-NN reaches -13.72 dB, improving by 2.26 dB over CP (≈ -11.46 dB), 4.80 dB over Tucker (≈ -8.93 dB), and 5.85 dB over LMMSE (≈ -7.87 dB). At $\rho = 20\%$, Tensor-NN remains best (≈ -18.43 dB), with a 1.00 dB margin over CP (≈ -17.43 dB). CP exhibits severe heavy-tail instability at $\rho = 2\%$ (mean NMSE $\approx +13.96$ dB), while Tensor-NN remains stable throughout.
4. **Algebraic structure consistently outperforms unconstrained deep learning.** The comparison with the ResNet baseline in Fig. 6 shows that Tensor-NN outperforms ResNet at every pilot density tested, with a monotonically growing margin: 1.53 dB at $\rho = 2\%$, 3.64 dB at $\rho = 4\%$, 3.58 dB at $\rho = 6\%$, 3.67 dB at $\rho = 8\%$, 3.91 dB at $\rho = 10\%$, 4.91 dB at $\rho = 15\%$, and 5.67 dB at $\rho = 20\%$. The global SNR reference of (16) ensures that the advantage of algebraic structure is not an artefact of the measurement setting. The monotonically growing gap indicates that structure-informed estimation scales more efficiently with pilot density than unconstrained learning, which is ultimately bounded by training data diversity rather than intrinsic channel geometry. These results demonstrate that the algebraic prior is the dominant source of performance gain across the full pilot-density range, and that the neural residual stage provides complementary correction for model mismatch rather than compensating for insufficient structure.
5. **Sample complexity is governed by intrinsic channel structure.** Experiment 4 shows that the minimum pilot ratio ρ_{\min} and observation count $|\Omega|_{\min}$ increase monotonically with the number of propagation paths L . At SNR = 10 dB, no configuration reaches $\text{NMSE} \leq 10^{-2}$ within the tested range, indicating a noise-limited regime where increasing pilot density alone cannot compensate for measurement noise. For SNR $\in \{20, 30\}$ dB, recovery thresholds lie in the 12–25% pilot range and are primarily governed by L rather than by the ambient tensor dimension $N_r N_t N_f$, consistent with Table 3.

5.7 Limitations

Despite the gains reported above, the proposed framework has limitations that merit explicit discussion:

- **Rank selection and sensitivity.** The tensor methods require multilinear ranks (or CP rank) specified a priori. The current implementation fixes ranks per experiment and, in the sample-complexity study, ties them to the number of paths via $(R_r, R_t, R_f) = (L, L, L+1)$. Performance degrades under rank mismatch, and a principled, data-driven rank selection strategy remains necessary for robust deployment.
- **High-mobility and time-varying channels.** The experiments assume quasi-static channels and single-snapshot estimators. Rapid mobility, Doppler spread, and temporal correlation fall outside the model; extending the framework to spatio-temporal estimation or channel tracking remains future work.
- **Neural training requirements.** The neural components (Tensor-NN residual and ResNet baselines) train offline on paired $(\mathcal{H}, \mathcal{Y}_\Omega)$ data under multi-SNR and multi-pilot regimes. Deployment may require representative training data (or synthetic surrogates) and fine-tuning to mitigate distribution shift across scenarios, environments, or array configurations.

- **Synchronization and hardware impairments.** The observation model covers only entry-wise sampling with additive Gaussian noise. Effects such as carrier-frequency offset, phase noise, IQ imbalance, nonlinear power amplifiers, low-resolution quantization, and other hardware imperfections fall outside the model. Their impact on tensor completion and neural residual learning remains an open question.

5.8 Reproducibility

All experiments ran on a Lenovo laptop (Intel Core i7, 16 GB RAM, NVIDIA GeForce RTX 2060 6 GB GPU) under Python 3.10 with PyTorch 2.1. A fixed random seed (`base_seed=42`) ensures deterministic channel generation, pilot sampling, and network initialization across all experiments.

The complete codebase—including data generation scripts, training configurations, pretrained model checkpoints, and plotting utilities—is publicly available at:

<https://github.com/alexandreblima/MIMO-TN>

The experiments generate DeepMIMO channels using the official dataset API [34] with configuration files provided in the repository. Researchers can reproduce all figures and tables by executing the provided shell scripts with default parameters.

6 Conclusion

This paper proposed a structure-informed framework for pilot-limited wideband MIMO channel estimation combining low-rank tensor completion with neural residual learning. The formulation directly addresses the ill-posed inverse problem induced by sparse pilot observations by exploiting algebraic priors that arise universally from sparse multipath propagation and array geometry, without requiring site-specific environmental models. SNR is defined globally with respect to the average power per channel coefficient over the full tensor—independent of the pilot set Ω and pilot ratio ρ —ensuring strict comparability across all experiments and pilot densities.

Synthetic-channel experiments demonstrate that Tucker completion achieves 10.88 dB NMSE improvement over LS and 7.83 dB over OMP at $\rho = 10\%$ pilot density. CP outperforms Tucker across the full SNR range under the specular multipath model, reaching a 13.11 dB advantage at SNR = 20 dB, consistent with the rank-one multipath structure that matches the CP parameterization exactly. On DeepMIMO ray-tracing channels, CP maintains its advantage over Tucker for $\rho \geq 6\%$ but exhibits severe heavy-tail divergence at $\rho = 2\%$ (mean NMSE $\approx +13.96$ dB), where Tucker’s alternating-projection scheme remains numerically stable. The proposed Tensor-NN estimator achieves 2.26 dB gain over CP and 4.80 dB over Tucker at $\rho = 8\%$, and outperforms the purely data-driven ResNet baseline at every pilot density tested, with a monotonically growing margin from 1.53 dB at $\rho = 2\%$ to 5.67 dB at $\rho = 20\%$. This result confirms that algebraic structure is the dominant source of performance gain across the full pilot-density range, and that the neural residual stage provides complementary correction for model mismatch rather than substituting for structural priors.

Empirical recovery thresholds confirm that the minimum observation count scales primarily with intrinsic channel complexity—governed by the number of dominant propagation paths L —rather than with the ambient tensor dimension $N_r N_t N_f$. At SNR ≥ 20 dB, channels with up to 15 dominant paths admit reliable recovery with 12–25% pilot density.

These findings establish tensor priors as physically grounded, portable, and theoretically motivated constraints for pilot-limited estimation, while neural residual learning provides a principled mechanism to compensate model mismatch under realistic propagation conditions. Future work will address adaptive rank

selection via model-order estimation, extensions to time-varying channels through joint space–frequency–time tensor modeling, integration with hybrid analog-digital architectures, and robustness analysis under hardware impairments including phase noise, nonlinearities, and low-resolution quantization.

References

- [1] T. L. Marzetta, E. G. Larsson, H. Yang, and H. Q. Ngo, *Fundamentals of Massive MIMO*. Cambridge University Press, 2016.
- [2] R. W. Heath, N. Gonzalez-Prelcic, S. Rangan, W. Roh, and A. M. Sayeed, “An overview of signal processing techniques for millimeter wave MIMO systems,” *IEEE journal of selected topics in signal processing*, vol. 10, no. 3, pp. 436–453, 2016.
- [3] E. Björnson, J. Hoydis, L. Sanguinetti *et al.*, “Massive mimo networks: Spectral, energy, and hardware efficiency,” *Foundations and Trends in Signal Processing*, vol. 11, no. 3-4, pp. 154–655, 2017.
- [4] E. Björnson, L. Sanguinetti, H. Wymeersch, J. Hoydis, and T. L. Marzetta, “Massive mimo is a reality—what is next?: Five promising research directions for antenna arrays,” *Digital Signal Processing*, vol. 94, pp. 3–20, 2019.
- [5] F. Liu, Y. Cui, C. Masouros, J. Xu, T. X. Han, Y. C. Eldar, and S. Buzzi, “Integrated sensing and communications: Toward dual-functional wireless networks for 6g and beyond,” *IEEE journal on selected areas in communications*, vol. 40, no. 6, pp. 1728–1767, 2022.
- [6] X. Rao and V. K. N. Lau, “Distributed compressive CSIT estimation and feedback for FDD multi-user massive MIMO systems,” *IEEE Transactions on Signal Processing*, vol. 62, no. 12, pp. 3261–3271, 2014.
- [7] A. Alkhateeb, O. El Ayach, G. Leus, and R. W. Heath, “Channel estimation and hybrid precoding for millimeter wave cellular systems,” *IEEE journal of selected topics in signal processing*, vol. 8, no. 5, pp. 831–846, 2014.
- [8] H. He, C.-K. Wen, S. Jin, and G. Y. Li, “Deep learning-based channel estimation for beamspace mmWave massive MIMO systems,” *IEEE Wireless Communications Letters*, vol. 7, no. 5, pp. 852–855, 2018.
- [9] M. Soltani, V. Pober, M. Doroslovacki, and R. M. Buehrer, “Deep learning-based channel estimation,” *IEEE Communications Letters*, vol. 23, no. 4, pp. 652–655, 2019.
- [10] M. Boloursaz Mashhadi and D. Gündüz, “Deep learning for massive MIMO channel state acquisition and feedback,” *Journal of the Indian Institute of Science*, vol. 100, no. 2, pp. 369–382, 2020.
- [11] J. Guo, T. Chen, S. Jin, G. Y. Li, X. Wang, and X. Hou, “Deep learning for joint channel estimation and feedback in massive MIMO systems,” *Digital Communications and Networks*, vol. 10, no. 1, pp. 83–93, 2024.
- [12] J. Gao, C. Zhong, G. Y. Li, and Z. Zhang, “Deep learning-based channel estimation for massive mimo with hybrid transceivers,” *IEEE Transactions on Wireless Communications*, vol. 21, no. 7, pp. 5162–5174, 2021.
- [13] G. E. Karniadakis, I. G. Kevrekidis, L. Lu, P. Perdikaris, S. Wang, and L. Yang, “Physics-informed machine learning,” *Nature Reviews Physics*, vol. 3, no. 6, pp. 422–440, 2021.

- [14] Y. He, N. Xu, L. Cheng, and H. Yuan, "Attention-guided wireless channel modeling and generating," *Applied Sciences*, vol. 15, no. 6, p. 3058, 2025.
- [15] B. Böck, A. Oeldemann, T. Mayer, F. Rossetto, and W. Utschick, "Physics-informed generative modeling of wireless channels," *arXiv preprint arXiv:2502.10137*, 2025.
- [16] N. D. Sidiropoulos, L. De Lathauwer, X. Fu, K. Huang, E. E. Papalexakis, and C. Faloutsos, "Tensor decomposition for signal processing and machine learning," *IEEE Transactions on Signal Processing*, vol. 65, no. 13, pp. 3551–3582, 2017.
- [17] Z. Zhou, J. Fang, L. Yang, H. Li, Z. Chen, and R. S. Blum, "Low-rank tensor decomposition-aided channel estimation for millimeter wave MIMO-OFDM systems," *IEEE Journal on Selected Areas in Communications*, vol. 35, no. 7, pp. 1524–1538, 2017.
- [18] A. Auddy, D. Xia, and M. Yuan, "Tensors in high-dimensional data analysis: Methodological opportunities and theoretical challenges," *Annual review of statistics and its application*, vol. 12, no. 1, pp. 527–551, 2025.
- [19] D. S. Rocha, G. Favier, and C. A. R. Fernandes, "Closed-form receiver for multi-hop MIMO relay systems with tensor space-time coding," *Journal of Communication and Information Systems*, vol. 34, no. 1, pp. 50–54, 2019.
- [20] R. Zhang, L. Cheng, S. Wang, Y. Lou, W. Wu, and D. W. K. Ng, "Tensor decomposition-based channel estimation for hybrid mmWave massive MIMO in high-mobility scenarios," *IEEE Transactions on Communications*, vol. 70, no. 9, pp. 6325–6340, 2022.
- [21] R. W. Heath Jr and A. Lozano, *Foundations of MIMO communication*. Cambridge University Press, 2018.
- [22] E. Candes and B. Recht, "Exact matrix completion via convex optimization," *Communications of the ACM*, vol. 55, no. 6, pp. 111–119, 2012.
- [23] T. G. Kolda and B. W. Bader, "Tensor decompositions and applications," *SIAM Review*, vol. 51, no. 3, pp. 455–500, 2009.
- [24] L. De Lathauwer, B. De Moor, and J. Vandewalle, "A multilinear singular value decomposition," *SIAM Journal on Matrix Analysis and Applications*, vol. 21, no. 4, pp. 1253–1278, 2000.
- [25] K. F. Masood, J. Tong, J. Xi, J. Yuan, Q. Guo, and Y. Yu, "Low-rank matrix sensing-based channel estimation for mmWave and THz hybrid MIMO systems," *IEEE Journal of Selected Topics in Signal Processing*, vol. 17, no. 4, pp. 777–793, 2023.
- [26] J. Liu, P. Musialski, P. Wonka, and J. Ye, "Tensor completion for estimating missing values in visual data," *IEEE transactions on pattern analysis and machine intelligence*, vol. 35, no. 1, pp. 208–220, 2012.
- [27] K. Gregor and Y. LeCun, "Learning fast approximations of sparse coding," in *Proceedings of the 27th International Conference on Machine Learning (ICML)*, 2010, pp. 399–406.
- [28] V. Monga, Y. Li, and Y. C. Eldar, "Algorithm unrolling: Interpretable, efficient deep learning for signal and image processing," *IEEE Signal Processing Magazine*, vol. 38, no. 2, pp. 18–44, 2021.
- [29] H. He, S. Jin, C.-K. Wen, F. Gao, G. Y. Li, and Z. Xu, "Model-driven deep learning for physical layer communications," *IEEE Wireless Communications*, vol. 26, no. 5, pp. 77–83, 2019.

- [30] O. Ronneberger, P. Fischer, and T. Brox, “U-net: Convolutional networks for biomedical image segmentation,” in *International Conference on Medical image computing and computer-assisted intervention*. Springer, 2015, pp. 234–241.
- [31] D. P. Kingma and J. Ba, “Adam: A method for stochastic optimization,” in *International Conference on Learning Representations (ICLR)*, 2015. [Online]. Available: <https://arxiv.org/abs/1412.6980>
- [32] A. Paszke, S. Gross, F. Massa, A. Lerer, J. Bradbury, G. Chanan, T. Killeen, Z. Lin, N. Gimelshein, L. Antiga *et al.*, “Pytorch: An imperative style, high-performance deep learning library,” *Advances in neural information processing systems*, vol. 32, 2019.
- [33] E. J. Candès and Y. Plan, “Matrix completion with noise,” *Proceedings of the IEEE*, vol. 98, no. 6, pp. 925–936, 2010.
- [34] A. Alkhateeb, “DeepMIMO: A generic deep learning dataset for millimeter wave and massive MIMO applications,” *arXiv preprint arXiv:1902.06435*, 2019, available: <https://deepmimo.net>.
- [35] K. He, X. Zhang, S. Ren, and J. Sun, “Deep residual learning for image recognition,” in *Proceedings of the IEEE conference on computer vision and pattern recognition*, 2016, pp. 770–778.
- [36] D. Burghal, Y. Li, P. Madadi, Y. Hu, J. Jeon, J. Cho, A. F. Molisch, and J. Zhang, “Enhanced AI-based CSI prediction solutions for massive MIMO in 5G and 6G systems,” *IEEE Access*, vol. 11, pp. 117 810–117 825, 2023.
- [37] P. Barman, V. Dehalwar, and R. Pateriya, “CSI Prediction for 5G and B5G in mMIMO System using Deep Learning Approach,” in *2025 IEEE Future Networks World Forum (FNWF)*. IEEE, 2025, pp. 1–6.
- [38] C. Cai, G. Li, H. V. Poor, and Y. Chen, “Nonconvex low-rank tensor completion from noisy data,” *Operations Research, INFORMS*, vol. 70, no. 2, pp. 1219–1237, 2021.